

Multi-frequency identification of defects in conducting media

A Pirani¹, M Ricci¹, R Specogna², A Tamburrino³ and F Trevisan²

¹ Polo Scientifico Didattico di Terni, Università degli Studi di Perugia, Via Pentima Bassa 21, Terni 05100, Italy

² Dipartimento di Ingegneria Elettrica, Gestionale e Meccanica, Università degli Studi di Udine, Via delle Scienze 208, Udine 33100, Italy

³ Ass EURATOM/ENEA/CREATE, DAEIMI, Università degli Studi di Cassino, Via G Di Biasio 43, Cassino 03043, Italy

E-mail: alessandro.pirani@unipg.it, marco.ricci@unipg.it, ruben.specogna@uniud.it, tamburrino@unicas.it and trevisan@uniud.it

Received 26 July 2007, in final form 18 March 2008

Published 16 April 2008

Online at stacks.iop.org/IP/24/035011

Abstract

An eddy currents based procedure for the 3D image reconstruction of defects in metallic plates from multi-frequency data is presented. In particular, we exploit the collection of data at different probe positions as well as at different excitation frequencies in order to improve the amount of information content, the accuracy of the inverse methodology and its robustness against the experimental noise. The identification tool we developed, exploits the *geometric $A - \chi$ formulation* for the solution of the eddy-current forward problem together with a full nonlinear iterative inversion algorithm based on the *total variation regularization*.

(Some figures in this article are in colour only in the electronic version)

1. Introduction

The eddy currents non-destructive technique (ECT) relies on the capability of a low-frequency electromagnetic field to penetrate and interact with conductive materials. For prescribed sources, measurements of field component values and of impedance variations allow us to image the conductivity inside materials. In this paper, we address the problem of 3D defects identification in metallic structures by ECT. This finds a wide application in the energy, automotive, marine, aeronautic and manufacturing industries.

The identification of the conductivity profile inside a material is seriously hampered by the inherently ill-posed and nonlinear nature of the eddy currents inverse problem (see [1–3] for mathematical issues); several techniques have been developed to solve it. Among them,

for the sake of completeness, we mention linear and quadratic models for approximating the forward problem, deterministic and stochastic algorithms, pre-calculated database, statistical methods, etc (see [4–15] and references therein).

In the present work, we tackle the inverse problem by combining the Gauss–Newton iterative method with the total variation (TV) by assuming that the anomalies are well approximated by a piecewise constant electrical conductivity distribution (see [16–21] for the application of the GN method and TV regularization, respectively). TV is a type of edge-preserving regularization and it is well suited to reconstructing blocky images; as quoted in [22] ‘... although Tikhonov-type regularization provides a good method to reconstruct smooth parameters both in terms of contrast and shape, it fails to reconstruct the sharp edges and absolute values for the high contrast case. TV regularization is a more suitable method for both sharp edges and high contrast’. This is the case for the specific applications considered in this paper, where it is reasonable to assume that the anomalies are modeled by a piecewise constant electrical conductivity.

Applications of TV to eddy-current imaging have been considered by several authors (e.g. [22–24] and references therein); the main problem highlighted in these works concerns the choice of the regularization parameter α . Either search-and-trial procedures or extensive numerical simulations [25] have been carried out to properly choose α . In addition, [23, 24] propose to include the TV regularization term in the multiplicative form $\Phi_{TV}(x) = \Phi(x)TV(x)$ instead of the usual additive form $\Phi_{TV}(x) = \Phi(x) + \alpha TV(x)$ (x being the unknown, Φ and Φ_{TV} being the discrepancy before and after regularization, TV denotes the total variation regularization term and α denotes the regularization parameter). The multiplicative approach allows us to overcome the problem of the choice of the regularization parameter, as evidenced by theoretical arguments and numerical examples.

In the present work, we adopt a different strategy consisting of applying the TV regularization to each single step of the GN method. In addition, in order to attain a full automation of the inverse procedure, we introduce a heuristic criterion for the choice of a proper regularization parameter α^* .

Together with the choice of a suitable regularization parameter α , the speed and accuracy of the forward solver are also of utmost importance: the (forward) modeling of signals from 3D defects (see, for instance, [7, 8, 12, 13, 28–30]) needs to be fast and accurate because inversion algorithms require the solution of a large number of forward problems and at the same time numerical errors may corrupt the information content of the data. In this paper, the forward problem solver ‘embedded’ in the imaging algorithm and used to generate the synthetic data is a full 3D formulation of the eddy-current problem based on a novel approach, i.e. on a reinterpretation of the finite element method in geometric terms. Such an approach, denoted as a discrete geometric approach, shifts emphasis from the Galerkin technique directly on the Maxwell equations and on the discrete counterparts of the constitutive relations. As a result, it becomes visible how the finite element kind of techniques solve approximately the basic equations of electromagnetism in terms of circulations and fluxes. (For a background of the discrete geometric approach, see [31–43]). The forward problem has also been validated against numerical and experimental data in [44].

In this paper, the data are collected at several probe positions and frequencies. The extension of the conventional multi-probe procedure to include multi-frequency signals, provides the following advantages [27, 39]:

- it offers the ability to assess profiles at different depths, since any frequency is associated with a specific skin-depth penetration δ ;
- it mitigates the ill-posedness by reducing the under-determination of the inverse problem.

The paper is structured as follows. In section 2, we describe the characteristics of the model adopted, while in section 3, we explain the geometric formulation used to solve the forward electromagnetic problem. Section 4 presents the inverse algorithm employed, while section 5 reports the numerical results. In section 6, we draw some conclusions and perspectives.

2. Model definition

We consider an aluminium plate with nominal electrical conductivity $\sigma_{Al} = 37.7 \times 10^6 \text{ S m}^{-1}$ and relative magnetic permeability $\mu_r \approx 1$. For the inverse problem, we focus on a restricted region of the plate modeled with a regular grid of $M = N_x \times N_y \times N_z$ cubes named ‘active voxels’ where N_x , N_y and N_z are the number of voxels in the x , y and z directions, respectively; the edge of each voxel is equal to 1 mm. A voxel represents the basic volumetric element of conducting material and we assign at each voxel a uniform value of the electrical conductivity. Real world defect presents a great variability in sizes. In this case, we have chosen the voxel dimension suitable to model real stress corrosion and cracks, e.g. in pipelines or in aircrafts.

In the following, we also introduce a fictitious division of the plate into N_z layers, where ‘layer 1’ indicates the one at the top, i.e. the scanning surface. Within the active voxel region we represent the defect as a well-defined number of voxels with a conductivity different from the background value σ_{Al} . We assume the defect homogeneous and well delimited inside the structure under study thus leading to a blocky conductivity distribution denoted with the array σ^* , whose k th component σ_k^* is the actual value of the electrical conductivity of the k th active voxel. Then the overall conductivity profile of the active region consists of a piecewise constant distribution of values with abrupt discontinuities in correspondence of the defect.

Our aim is to compute an approximation of σ^* starting from the knowledge of the array \hat{v}^* of the actual complex voltages of the driving-probe coil excited by a sinusoidal current generator at different positions and frequencies. The coil consists of 200 turns, with an outer radius of 2 mm, an inner radius of 0.5 mm, a height of 3 mm and a lift-off of 0.5 mm.

Henceforth we deal with two different geometric models:

Model (a): a 3 mm thick plate with $M = 14 \times 14 \times 3 = 588$ active voxels;

Model (b): a 4 mm thick plate with $M = 16 \times 16 \times 4 = 1024$ active voxels.

To guarantee a proper modeling of the plate mesh under all probe positions, we also consider a frame of ‘passive voxels’ around the active region. These passive voxels have the same geometric dimensions of the active ones, and therefore the same mesh refinement, but they are not processed in the solution of the inverse problem; their conductivity is fixed to the background value σ_{Al} .

The probe-coil assumes N_{pos} distinct positions properly spaced to guarantee a uniform covering of the active voxels region, while the number N_{freq} of excitation frequencies is equal to the number of layers in the z -direction and their corresponding penetration depths are linearly spaced and related to the layer depths. In this way, we assure a good trade-off between the total number of data to invert ($N = N_{freq} \times N_{pos}$) and the overall computational time, contextually providing a linear independence between the measurements, as assessed by a preliminary SVD analysis. Following the above frequency-choice criterion, in model (a) we adopt $N_{freq} = 3$ working frequencies of 6000 Hz, 1500 Hz and 670 Hz, with a penetration depth of δ_0 , $2\delta_0$ and $3\delta_0$ (with $\delta_0 \cong 1.1$ mm), respectively; in model (b) we adopt $N_{freq} = 4$ working frequencies of 6000 Hz, 1500 Hz, 670 Hz and 375 Hz, with the penetration depth of δ_0 , $2\delta_0$, $3\delta_0$ and $4\delta_0$, respectively. For both the models we move the probe-coil over $N_{pos} = 41$ different positions on the top of the plate, just above layer 1 (see figure 1), whose centers build

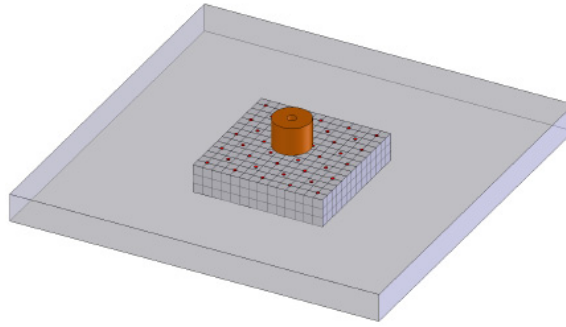


Figure 1. View of the probe-coil, the plate and the active voxel grid (model (a)). The red points represent the positions of the scan of the coil above the active voxel region.

up a regular array of points oriented at 45° with respect to the active voxels grid and equally spaced of $3/\sqrt{2} \cong 2$ mm corresponding to the outer coil radius.

3. Forward problem

In order to solve the eddy-current problem we resort to the so-called discrete geometric approach [31, 36, 40]. The domain of interest D of the eddy-current problem has been partitioned into a source region D_s consisting of a current driven coil, and a conductive region D_c . The complement of $D_c \cup D_s$ in D represents the air region D_a . In D a pair of interlocked cell complexes is introduced [31]. The primal complex \mathcal{K} is simplicial with *inner* oriented cells [36] such as nodes n , edges e , faces f , volumes v (v are tetrahedra).

The dual complex $\tilde{\mathcal{K}}$ is obtained from the primal one according to the barycentric subdivision, with *outer* oriented cells [36] such as dual volumes \tilde{v} , dual faces \tilde{f} , dual edges \tilde{e} , dual nodes \tilde{n} . For example a dual node \tilde{n} is the barycenter of the tetrahedron v , a dual edge \tilde{e} is the line drawn from the barycenter of f joining the two dual nodes \tilde{n}' , \tilde{n}'' in the tetrahedra v' , v'' on both sides of f . We define the mesh as $\mathcal{M} = (\mathcal{K}, \tilde{\mathcal{K}})$ (see figure 2). The interconnections between cells of the primal complex are defined by the usual connectivity matrices \mathbf{G} between pairs (e, n) , \mathbf{C} between pairs (f, e) , \mathbf{D} between pairs (v, f) . Similarly, the corresponding matrices for the dual complex are $-\mathbf{G}^T$ (the minus sign is due to the assumption that a dual volume \tilde{n} is oriented by the outward normal, while a node n is oriented as a sink) between pairs (\tilde{n}, \tilde{e}) , \mathbf{C}^T between pairs (\tilde{e}, \tilde{f}) and \mathbf{D}^T between pairs (\tilde{f}, \tilde{v}) .

Next, we consider the integrals of the field quantities, also referred to as *global variables*, for an eddy-current problem with respect to the oriented geometric elements of a mesh \mathcal{M} , yielding the degrees of freedom (DoF) arrays (denoted in boldface type); each entry of a DoF array is indexed over the corresponding geometric element. In this way, there is a unique association between a global variable and the corresponding geometric element.

Therefore, we denote with:

- Φ is the array of magnetic fluxes associated with primal faces in D ;
- \mathbf{F} is the array of magnetomotive forces (mmfs) associated with dual edges in D ;
- \mathbf{I} is the array of electric currents associated with dual faces and \mathbf{U} is the array of electromotive forces (emfs) associated with primal edges; they have non-null entries only for the dual faces and primal edges in D_s and D_c regions.

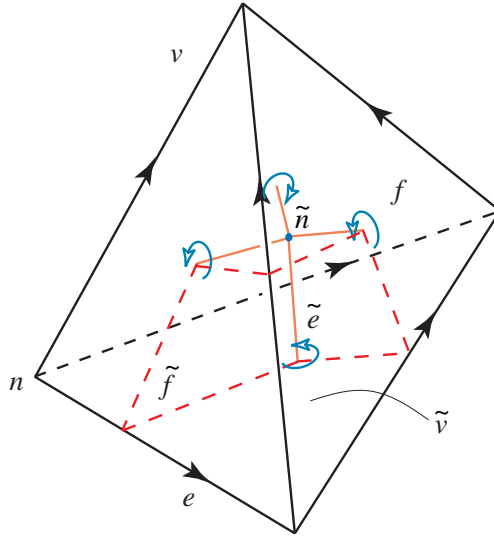


Figure 2. For clarity, the geometric elements of the pair of interlocked cell complexes $\mathcal{K}, \tilde{\mathcal{K}}$ are shown for the case of a mesh formed by a single tetrahedron. In particular the dual node \tilde{n} is the barycenter of the tetrahedron v and a dual edge \tilde{e} is a segment drawn between \tilde{n} and the barycenter of a primal face f .

With these definitions the algebraic version of Gauss' law, Ampere's law and Maxwell–Faraday law can be written as

$$\mathbf{D}\Phi = 0, \quad (1a)$$

$$\mathbf{C}^T \mathbf{F} = \mathbf{I}, \quad (1b)$$

$$\mathbf{C}\mathbf{U} = -\mathbf{i}\omega\Phi. \quad (1c)$$

Introducing the magnetic vector potential \mathbf{A} , we can define \mathbf{A}' as the array of the circulations of the magnetic vector potential along the primal edges of \mathcal{M} . The circulations \mathbf{A}' can be decomposed with $\mathbf{A}' = \mathbf{A} + \mathbf{G}\chi$, where χ is the array of electric scalar potential defined on the primal nodes of the conducting domain mesh. Using the magnetic vector potential, we can write $\Phi = \mathbf{C}(\mathbf{A} + \mathbf{G}\chi)$ and $\mathbf{U} = -\mathbf{i}\omega\mathbf{A} - \mathbf{i}\omega\mathbf{G}\chi$. Then the Gauss' law at discrete level become identically satisfied $\mathbf{D}\Phi = \mathbf{D}\mathbf{C}(\mathbf{A} + \mathbf{G}\chi) \equiv 0$, since in every mesh complex $\mathbf{D}\mathbf{C} \equiv 0$ and $\mathbf{C}\mathbf{G} \equiv 0$ hold. It is easy to see that the Faraday–Neumann law at discrete level is identically satisfied too: $\mathbf{C}\mathbf{U} = \mathbf{C}(-\mathbf{i}\omega\mathbf{A} - \mathbf{i}\omega\mathbf{G}\chi) = -\mathbf{i}\omega\mathbf{C}\mathbf{A} = -\mathbf{i}\omega\Phi$.

In addition to the physical laws, we need the discrete counterparts of the constitutive relations mapping a DoF array associated with a geometric entity of \mathcal{K} into the dual geometric entity of $\tilde{\mathcal{K}}$. The discrete constitutive laws can be written as

$$\mathbf{F} = \mathbf{M}_v \Phi, \quad (2a)$$

$$\mathbf{I} = \mathbf{M}_\sigma \mathbf{U}. \quad (2b)$$

The square matrix \mathbf{M}_v ($\dim(\mathbf{M}_v) = N_f$, N_f being the number of faces in \mathcal{K}) is the reluctance matrix such that (2a) holds exactly at least for element wise *uniform* induction field \mathbf{B} and magnetic field \mathbf{H} in each tetrahedron. \mathbf{M}_σ is a square matrix ($\dim(\mathbf{M}_\sigma) = \mathcal{E}_c$, \mathcal{E}_c being

the number of edges in D_c) that is the discrete counterpart of Ohm's constitutive pointwise relation.

Since algebraic Maxwell's laws involve only combinatorial information, the metric- and material-dependent properties enter only in the definition of the constitutive matrices.

Combining equations (1b) and (2) together with the continuity law $\mathbf{G}^T \mathbf{I} = 0$ we obtain the algebraic equations governing the Geometric $A - \chi$ formulation⁴ [38, 41], formulated in terms of the array \mathbf{A} of the circulations of the magnetic vector potential along primal edges e of D and in terms of the array χ of scalar potential χ associated with primal nodes n of D_c . We obtain

$$\begin{aligned} (\mathbf{C}^T M_v \mathbf{C} \mathbf{A})_e &= (\mathbf{I}_s)_e & \forall e \in D - D_c \\ (\mathbf{C}^T M_v \mathbf{C} \mathbf{A})_e + \mathbf{i}\omega (M_\sigma \mathbf{A}_c)_e + \mathbf{i}\omega (M_\sigma \mathbf{G} \chi)_e &= 0 & \forall e \in D_c, \\ \mathbf{i}\omega (\mathbf{G}^T M_\sigma \mathbf{A}_c)_n + \mathbf{i}\omega (\mathbf{G}^T M_\sigma \mathbf{G} \chi)_n &= 0 & \forall n \in D_c, \end{aligned} \quad (3)$$

where array \mathbf{A}_c is the sub-array of \mathbf{A} , associated with primal edges in D_c and \mathbf{I}_s is the array of the source currents crossing dual faces in D_s . With notation $(\mathbf{x})_k$, we mean the k th row of array \mathbf{x} , where $k = \{e, n\}$ is the label of edge e or of node n .

3.1. The constitutive matrices

The constitutive matrices M_v and M_σ can be constructed using different techniques described in [38, 40, 41, 45].

In this paper, we will resort to a novel energetic approach to build such matrices based on an energetic approach using the edge and face vector base functions defined in [42, 43]. This approach assures that symmetry, positive definiteness and consistency⁵ properties are satisfied for both the matrices M_v and M_σ .

3.2. Integral representation of sources

Thanks to the linearity of the media, we can express the array \mathbf{A} as $\mathbf{A} = \mathbf{A}_r + \mathbf{A}_s$, where \mathbf{A}_s is the array of circulations of the contribution to the magnetic vector potential produced by the source currents in D_s and \mathbf{A}_r is the array of circulations of the contribution to the magnetic vector potential due to the eddy-currents in D_c . Therefore we have that

$$\begin{aligned} (\mathbf{C}^T M_v \mathbf{C} \mathbf{A}_s)_e &= (\mathbf{I}_s)_e & (\mathbf{C}^T M_v \mathbf{C} \mathbf{A}_r)_e &= 0 & \forall e \in D_s \\ (\mathbf{C}^T M_v \mathbf{C} \mathbf{A}_s)_e &= 0 & (\mathbf{C}^T M_v \mathbf{C} \mathbf{A}_r)_e &= (\mathbf{I})_e & \forall e \in D_c \end{aligned} \quad (4)$$

holds, where \mathbf{I} is the array of eddy currents crossing \tilde{f} in D_c . Each entry $(\mathbf{A}_s)_i$ of the array \mathbf{A}_s can be pre-computed as $(\mathbf{A}_s)_i = \int_{e_i} \mathbf{A}_s \cdot d\mathbf{l}$, where e_i is a primal edge in D and \mathbf{A}_s is the magnetic vector potential due to the known source current density in D_s . In our case, we have a stranded circular coil and \mathbf{A}_s can be computed in closed form in terms of the elliptic integrals of the first and second kind [32, 46].

In this way, we can rewrite the system (3) by removing the source currents from its right-hand side, obtaining

$$\begin{aligned} (\mathbf{C}^T M_v \mathbf{C} \mathbf{A}_r)_e &= 0 & \forall e \in D - D_c \\ (\mathbf{C}^T M_v \mathbf{C} \mathbf{A}_r)_e + \mathbf{i}\omega (M_\sigma \mathbf{A}_c)_e + \mathbf{i}\omega (M_\sigma \mathbf{G} \chi)_e &= \mathbf{v} & \forall e \in D_c, \\ \mathbf{i}\omega (\mathbf{G}^T M_\sigma \mathbf{A}_c)_n + \mathbf{i}\omega (\mathbf{G}^T M_\sigma \mathbf{G} \chi)_n &= \mathbf{w} & \forall n \in D_c, \end{aligned} \quad (5)$$

⁴ This formulation is part of the geometric approach for Maxwell's equations (GAME) code developed by R Specogna and F Trevisan with the partial support of MIUR (Italian Ministry for University and Research), <http://www.quickgame.org>.

⁵ A precise definition of the notion of consistency for constitutive matrices is given in [32].

where $\mathbf{v} = -\mathbf{i}\omega(M_\sigma \mathbf{A}_{cs})_e$ and $\mathbf{w} = \mathbf{i}\omega(\mathbf{G}^T \mathbf{v})_e$. The symmetric linear system (5) is singular and to solve it we rely on the CG method without gauge condition.

3.2.1. Calculation of the induced voltage. For the calculation of the induced voltage we subdivide the coilpro in a series of M sub-coils. The voltage induced at the terminals of the i th sub-coil can be determined by

$$U_i = -\mathbf{i}\omega\Phi_i = -\mathbf{i}\omega N_i \int_{c_i} \mathbf{A} \cdot d\mathbf{l}, \quad (6)$$

where c_i is the circumference coaxial with the coil and passing through the barycenter of the considered sub-coil. For the calculation of the integral we use the Biot–Savart law,

$$\mathbf{A}(P) = \mathbf{A}_s(P) + \frac{\mu_0}{4\pi} \int_{D_c} \frac{\mathbf{J}(P')}{|P - P'|} dV. \quad (7)$$

4. Inverse problem

The eddy currents inside a voxel, for a fixed coil current, position and frequency, depend on the conductivity of a number of neighboring voxels. Thence the inverse problem is inherently nonlinear. Denoting with \dot{v} the complex voltages array consisting of the probe voltages collected at different excitation frequencies and positions, the dependence of \dot{v} on the conductivity distribution can be expressed as

$$\dot{v} = F(\sigma), \quad (8)$$

where F is a nonlinear complex operator and σ is the array of the values of the conductivity in the active voxels.

The inverse problem aims at estimating the actual conductivity distribution σ^* from the knowledge of the complex data array \dot{v}^* , in general affected by noise (see section 5 for the noise model adopted in this work). The proposed algorithm is based on the Gauss–Newton (GN) method, an iterative method where the update σ^{n+1} at step $n + 1$ is obtained from σ^n as $\sigma^{n+1} = \sigma^n + \delta\sigma^n$ where $\delta\sigma^n$ is a solution of

$$\dot{v}^* = F(\sigma^n) + \dot{S}^n \delta\sigma^n, \quad (9)$$

with \dot{S}^n being the Jacobian of F at point σ^n .

Due to its underlying ill-posedness, problem (9) requires to be regularized. The regularization topic has attracted the interest of many researchers in the last decades, e.g. [18, 47–49], and many regularization schemes have been proposed. Our problem is characterized by a conductivity that is prevalently blocky; therefore, our choice falls on the total variation (TV) regularization, complying with this assumption [17]. TV is essentially based on a L^1 -norm of derivatives, thus it measures the discontinuities in the image data set and preserves edge informations without any prior knowledge about the blurred image geometric details [19, 25]. The solution $\delta\sigma^n$ of (9) is taken as the minimum of the following functional:

$$\begin{aligned} \mathcal{E}_{TV}^n(\delta\sigma) &= \|\delta\dot{v}^n - \dot{S}^n \delta\sigma^n\|^2 + \alpha TV(\sigma^n + \delta\sigma), \\ \delta\dot{v}^n &= \dot{v}^* - F(\sigma^n), \end{aligned} \quad (10)$$

where α is the regularization parameter and

$$TV(\sigma) = \frac{1}{2} \sum_{k=1}^M \psi(|D_k^x \sigma|^2 + |D_k^y \sigma|^2). \quad (11)$$

In (11) $D_k^x \sigma$ and $D_k^y \sigma$ are finite difference approximations of the ∂_x and ∂_y operators, $\psi(\xi)$ is a smooth approximation of the absolute value function $|\xi|$, introduced to avoid discontinuity of the derivative at $\xi = 0$ (we choose $\psi(g) = 2\sqrt{g^2 + \gamma^2}$, where $\gamma > 0$ is a small parameter) [18]. The expression on the right-hand side of (11) is a discrete approximation of the continuous TV penalty term⁶,

$$\int \sqrt{|\partial_x \sigma(x, y, z)|^2 + |\partial_y \sigma(x, y, z)|^2} dV, \quad (12)$$

with $\sigma(x, y, z)$ being the conductivity distribution represented by the array σ .

Another available *a priori* information is that the conductivity of the k th voxel falls in the range $[0, \sigma_{Al}]$. This implies that a defect acts as either a partial ($0 < \sigma_k < \sigma_{Al}$) or a total barrier ($\sigma_k = 0$) to the circulation of the electrical current. We have taken into account this constraint by introducing a projection operator P [48]. Specifically, $P : \sigma \rightarrow \tilde{\sigma}$ is (componentwise) defined as

$$(P\sigma)_k = \begin{cases} 0 & \text{if } \sigma_k < 0 \\ \sigma_k & \text{if } 0 \leq \sigma_k \leq \sigma_{Al} \\ \sigma_{Al} & \text{if } \sigma_{Al} < \sigma_k. \end{cases} \quad (13)$$

In summary, the algorithm reads:

- (i) set $n = 1$ and σ^n equal to the initial guess;
- (ii) find the minimizer $\delta\sigma^n$ of \mathcal{E}_{TV}^n ;
- (iii) update the solution as $\sigma^{n+1} = P[\sigma^n + \delta\sigma^n]$;
- (iv) increase n and go to step (ii) until convergence is achieved.

The minimization of (10) does not admit a closed form expression and an iterative minimization procedure is needed. Different strategies can be pursued to accomplish this aim [50]. We adopted the *lagged diffusivity fixed point iteration method* introduced by Vogel and Oman [18, 51, 52]. Then, at each n th iteration of the overall iterative minimization process (step (ii)), the minimization of \mathcal{E}_{TV}^n performs iterations henceforth labeled by using the index m .

4.1. Choice of the regularization parameter

In solving regularized ill-posed inverse problems, the choice of a suitable regularization parameter α is of utmost importance and several methods have been proposed to tackle this problem [18, 26, 47–49, 53]. Moreover due to the non-closed solution of the TV penalized least-squares problem, the determination of the optimal TV stop criterion plays a fundamental role. In this work we let both α and m vary in a fixed range of values; hence, we find the optimal parameters by taking the coordinates (α^*, m^*) corresponding to the global minimum of the functional (10) in the spanned range of parameters. A sketch of typical error trend is depicted in figure 3(left) where we report results concerning a large set of α values. We note that the minimum is achieved in few iterations for the index m . Moreover we have analyzed the relation existing between the optimal regularization parameter α^* and α_{eq} at the iteration n , where α_{eq} is defined as the value that balances the discrepancy term and the TV term in (10),

$$\alpha_{eq}^n = \frac{\|\delta\dot{v}^n\|_2^2}{TV(\sigma^n)}. \quad (14)$$

⁶ In this work, we assume a layer-by-layer regularization (the ∂_z operator has not been considered in (12)). This corresponds to defects having independent growth in each layer.

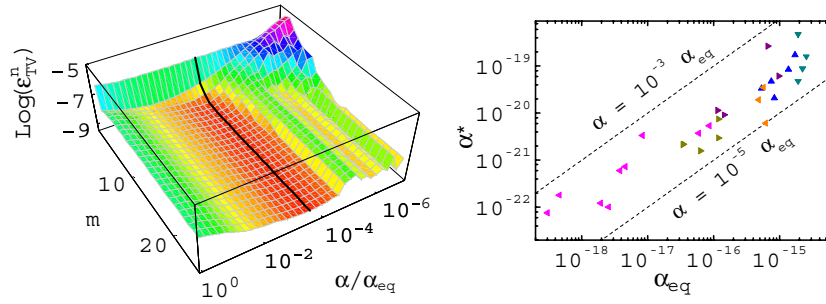


Figure 3. (Left) Typical 3D surface of the functional \mathcal{E}_{TV}^n : the black line indicates the value $\alpha = \alpha^*$. (Right) Plot of α^* versus α_{eq} : each color refers to a different configuration (defect type, noise level), see section 5.

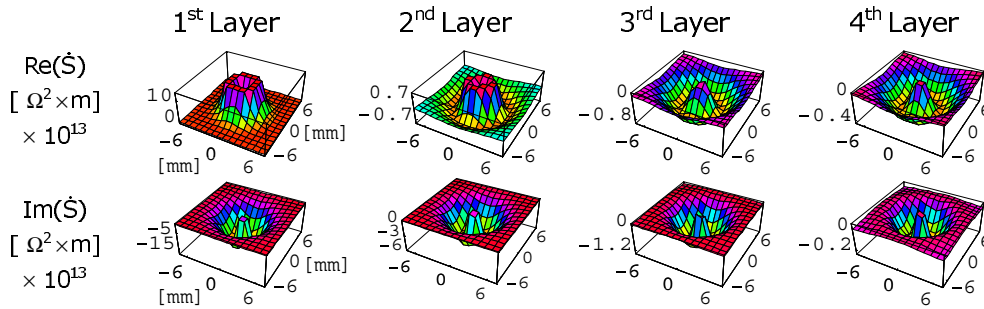


Figure 4. Example of sensitivity distributions for model (b), having fixed the frequency at 1500 Hz and the coil position in the center of the active voxels region.

By testing a wide variety of defect types and noise levels, for both models (a) and (b), we note that the optimal value α^* falls in the range $10^{-5}\alpha_{eq} \leq \alpha \leq 10^{-3}\alpha_{eq}$, as illustrated in figure 3(right).

4.2. Derivation of the sensitivity matrix

The complex sensitivity matrix \hat{S} of the voltages \hat{v} to small changes in conductivity of the k th active voxel is defined as

$$\hat{S}_{ik} = \frac{\partial \hat{v}_i}{\partial \sigma_k}. \tag{15}$$

It was found [54, 55] that for the present eddy currents problem, assuming the exciting coil coinciding with the measuring probe one and an unitary excitation current, \hat{S}_{ik} can be computed by means of the following compact expression:

$$\hat{S}_{ik} = - \int_{\Omega_k} \mathbf{E}_i \cdot \mathbf{E}_i \, d\Omega_k, \tag{16}$$

where \mathbf{E}_i is the electric field vector for the measurement configuration producing \hat{v}_i .

Figure 4 reports an example of sensitivity distributions, obtained for model (b) at frequency 1500 Hz and the probe in the 21st position (i.e. the coil placed in the center of the active voxels

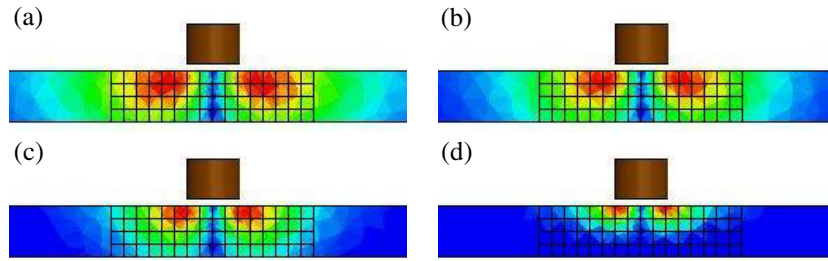


Figure 5. Model (b)—qualitative plots of the distribution of the magnitude of the eddy-current density in the section of the metallic plate (perpendicular to the plane of the probe scan) at each working frequency (probe position at the center of the active voxels region): (a) 375 Hz, (b) 670 Hz, (c) 1500 Hz and (d) 6000 Hz. In each subfigure the color bar is rescaled to fit its range of values.

region, see figure 1). In particular, we distinguish eight sub-figures. Taking into account the subdivision in four layers of voxels, we plot along the z axis the value of the real and imaginary parts of sensitivity matrix in the first and the second rows, respectively. The amplitude of the sensitivity values is high in correspondence of the coil outer radius and tends gradually to zero increasing the distance from the coil axis or approaching it. Moreover, superficial layers present higher sensitivity values than the inner ones, according to the skin effect. This means, as well known, that the spatial resolution of eddy-current testing depends not only on the working frequency but also on the depth of inspection.

4.3. Multi-frequency excitation and related SVD normalization

To enhance the 3D reconstruction capability of our methodology, we excite the system at N_{freq} different frequencies for each coil position, in order to gather a sufficient number of data that makes the inversion procedure reliable. Referring to model (b), figure 5 reports the vertical cross-section of the plate, with a sketch of the active voxels grid and also a qualitative plot of the eddy currents distribution at each excitation frequency, for the probe-coil placed in the 21st position (center of the active voxels region). These plots indicate that the actual values of the penetration depth are in agreement with the predicted ones (see section 2): in particular, at 375 Hz the eddy currents penetrate through all plate thickness, and so all the voxels layers, while at 6000 Hz we have significant currents only for the first two layers of voxels. Therefore, adopting solely a frequency of 6000 Hz, we have a nonzero sensitivity limited to the superficial layers, thus leading to unstable reconstruction of the inner layers. At the same time, regarding superficial layers, higher frequencies provide better resolutions and signal levels than lower ones. The adoption of a multi-frequency excitation allows us to balance these opposite aspects. However, measurements at different frequencies exhibit different signal amplitudes: the amplitude increases with the frequency. Then the highest frequency dominates the overall discrepancy, hiding the information content provided by the other frequencies. To avoid this unwanted behavior of the imaging procedure, we introduce a suitable normalization of the data [56]. In the literature, different choices for the weights can be found. For example in [12] they are inversely proportional to the square of the voltages at frequency j . In the present work, we propose a slightly different criterion based on the singular value decomposition (SVD) of the sensitivity matrix. Specifically, the data and discrepancy

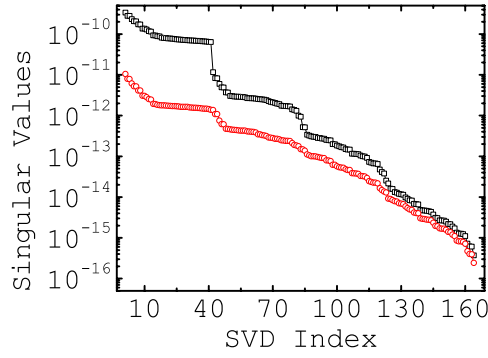


Figure 6. Model (a)—example of trends of the singular values of \dot{S} before (black marks) and after (red marks) the SVD normalization.

are weighted as follows:

$$\begin{aligned}
 \delta \dot{v}^n &\rightarrow \mathbf{w} \delta \dot{v}^n, \\
 \dot{S}^n &\rightarrow \mathbf{w} \dot{S}^n, \\
 \|\delta \dot{v}^n - \dot{S}^n \delta \sigma^n\|^2 &\rightarrow (\delta \dot{v}^n - \dot{S}^n \delta \sigma^n)^H \mathbf{w}^T \mathbf{w} (\delta \dot{v}^n - \dot{S}^n \delta \sigma^n).
 \end{aligned}
 \tag{17}$$

In (17) \mathbf{w} is a (real) diagonal matrix whose elements referring to the j th frequency are independent from the position index and inversely proportional to the part of the sensitivity matrix \dot{S} (the sensitivity matrix for the defect-free configuration) corresponding to the same j th frequency. As example, in case we have only two frequencies, \dot{S} can be partitioned as a column vector of two submatrices (one for each set of measurements at a prescribed frequency)

$$\dot{S} = \begin{bmatrix} \dot{S}_1 \\ \dot{S}_2 \end{bmatrix}$$

and

$$\mathbf{w} = \text{diag} \left[\overbrace{\lambda_1^{-1}, \dots, \lambda_1^{-1}}^{N_1}, \overbrace{\lambda_2^{-1}, \dots, \lambda_2^{-1}}^{N_2} \right],$$

where N_j and λ_j are the number of measurements and the largest singular value of \dot{S}_j , respectively, at the j th frequency.

Figure 6 reports the plots of the singular values of the matrix \dot{S} before and after the SVD normalization. We note that after the SVD normalization we have eliminated the gaps in the singular values, guaranteeing a better exploitation of the information content.

Finally, we would like to note that in perspective the experimental data to be processed could be attained by exploiting real multi-frequency excitation signals as in the case of pulsed eddy currents technique [57–60].

5. Numerical results

The data processed by the inversion algorithm are synthetic and generated by the same (full 3D) numerical model embedded in the imaging method. To avoid the inverse crime, the data

Table 1. Signal level and relative noise.

Freq. (Hz)	Signal level	Model (a)—type I			Signal level	Model (b)—type I		
		Relative noise				Relative noise		
		$\epsilon = 10^{-6}$	$\epsilon = 5 \times 10^{-6}$	$\epsilon = 10^{-5}$		$\epsilon = 10^{-6}$	$\epsilon = 5 \times 10^{-6}$	$\epsilon = 10^{-5}$
375	—	—	—	—	7.55×10^{-5}	14.74%	71.13%	147.42%
670	4.76×10^{-5}	2.57%	12.84%	25.40%	1.84×10^{-4}	6.25%	30.95%	62.54%
1500	1.74×10^{-4}	0.86%	4.29%	8.14%	4.49×10^{-4}	2.49%	13.01%	24.91%
6000	9.95×10^{-4}	0.19%	0.94%	1.85%	7.53×10^{-4}	1.88%	9.72%	18.78%

have been corrupted with a random generated noise. Basically, the eddy currents measuring systems implement a voltmeter, whose intrinsic noise depends on its operating range and accuracy. We have modeled this by introducing the noise in the following manner:

$$\begin{aligned}\dot{v}_i^* &= \dot{v}_i + \dot{\eta}_i, \\ \dot{\eta}_i &= \varepsilon \times V_i^{\text{air}} \times \rho_i \times e^{2\pi j \phi_i},\end{aligned}\quad (18)$$

where \dot{v}_i^* represents the noisy data, \dot{v}_i represents the noise-free data, $\dot{\eta}_i$ is the noise term, ε is a parameter that controls the magnitude of the noise, V_i^{air} is the coil voltage magnitude in air (in the absence of the conductive specimen) at the frequency competing to the i th measurement, ρ_i and ϕ_i are uniformly distributed random values on $[0, 1]$. It is worth noting that this can be considered a worst case scenario where the measurements are absolute, i.e. we measure the total voltage across the coil that includes: (i) the free-space contribution V^{air} , (ii) the eddy-current contribution due to the presence of the defect-free plate $\delta \dot{v}^{\text{plate}}$, (iii) the eddy-current contribution due to the presence of the defect $\delta \dot{v}^{\text{defect}}$. In the previous expressions $\sigma^{n=1}$ stands for the unflawed conductivity distribution (see section 4). In addition, taking into account the nominal parameters of the coil ($R^{\text{air}} = 1.18\Omega$, $L^{\text{air}} = 36\mu H$), the ratio between V^{air} at the highest frequency and V^{air} at the lowest frequency is about 1.5. This means the magnitude of the noise is rather flat in the considered frequency range (375–6000 Hz), thus the data at the lowest frequencies are relatively more penalized in term of noise.

To gain insight about signal and noise levels characterizing the present results, we introduce two quantities that relate the magnitude of this three terms with the noise contribute $\dot{\eta}$ for different values of the parameter ε . Precisely for each single frequency we define

$$\begin{aligned}\text{signal level} &= \frac{\max(|\delta \dot{v}_i^{\text{defect}}|)}{|V_i^{\text{air}}|}, \\ \text{relative noise} &= \frac{\|\dot{\eta}_i\|_2}{\|\delta \dot{v}_i^{\text{defect}}\|_2},\end{aligned}\quad (19)$$

where i is the overall measurement index, but related only to the measurements for a prescribed frequency. Table 1 reports some numerical values of these two quantities.

We note that a noise level ϵ of just few parts per million leads to a significant relative noise, especially for low frequencies as expected. This feature implies that model (b) is less robust towards noise than model (a) as well as deeper layers are less robust than superficial ones.

To stop the GN algorithm, we adopt a classical criterion for ill-posed problem (e.g. [48] and references therein). This criterion is based on the *a priori* knowledge of the noise level magnitude: the algorithm is stopped when the discrepancy goes below a threshold given by the product of a scaling factor (equal to 1.01 in this work and, in general, slightly larger than 1)

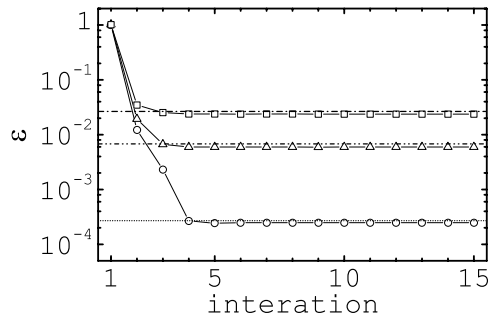


Figure 7. Model (a)—type I: discrepancy \mathcal{E} versus iteration number n . The plots refer to a noise level equal to $\epsilon = 10^{-6}$ (squares), $\epsilon = 5 \times 10^{-6}$ (triangles), $\epsilon = 10^{-5}$ (circles), respectively; the dotted lines indicates their corresponding threshold.

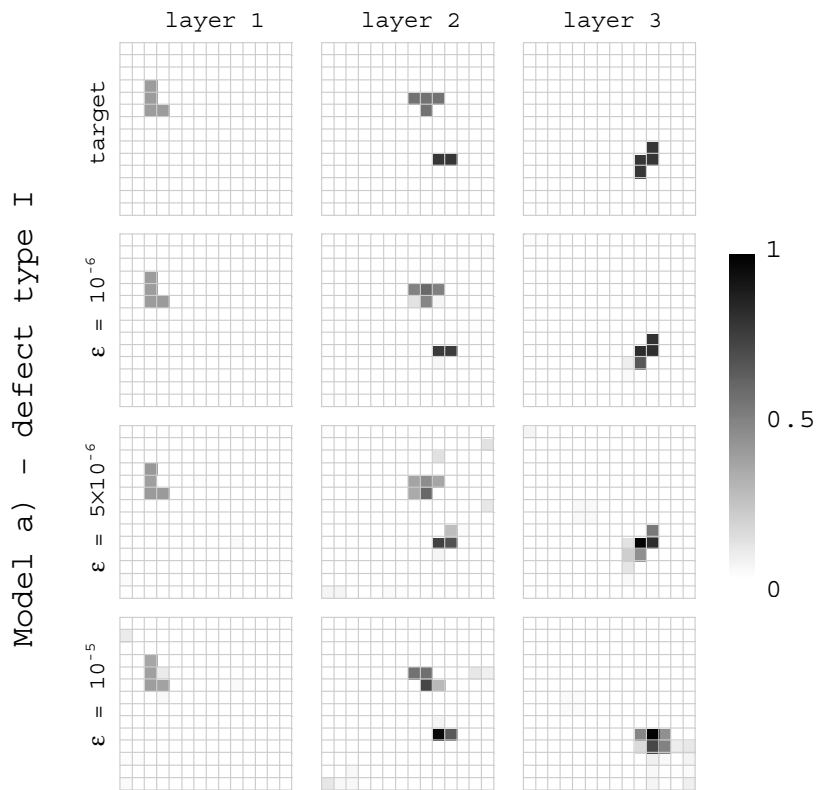


Figure 8. Images attained for model (a)—type I: the first row reports the target conductivity distribution; rows 2–4 report the distributions attained at the final iteration $n = 4, 3, 3$ and for $\epsilon = 10^{-6}, 5 \times 10^{-6}, 10^{-5}$, respectively.

and the magnitude of the noise energy. Figure 7 illustrates how such criterion works: the plots represent the trends of discrepancy versus the iteration number for different noise levels whereas the dotted lines indicate their corresponding thresholds. The results highlight that our method converges in few steps, as desirable in view of real world applications.

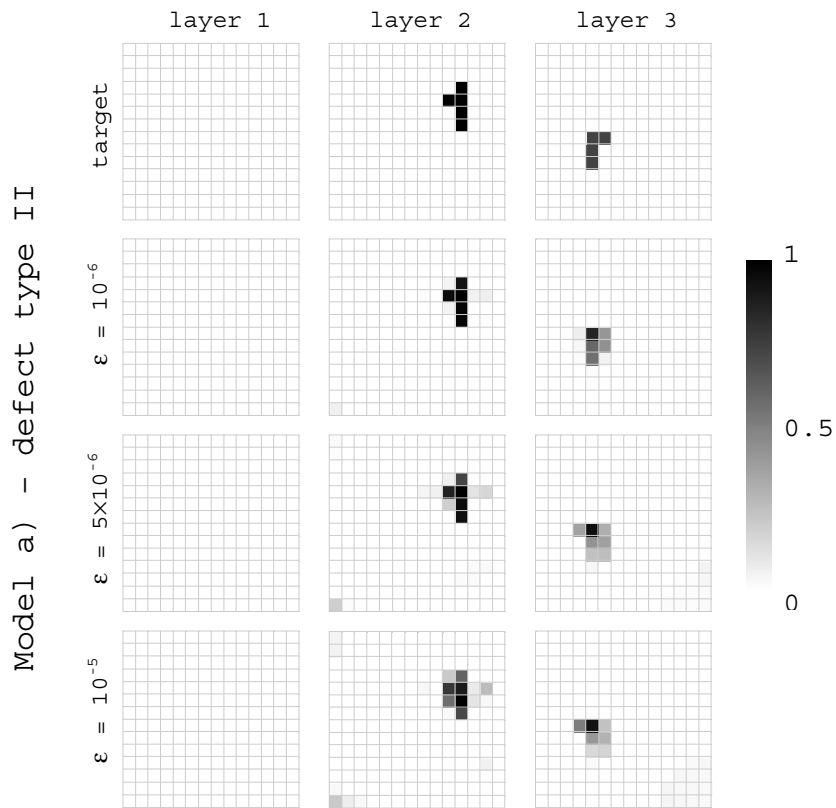


Figure 9. Images attained for model (a)—type I: the first row reports the target conductivity distribution; rows 2–4 report the distributions attained at the final iteration $n = 5, 4, 3$ and for $\epsilon = 10^{-6}, 5 \times 10^{-6}, 10^{-5}$, respectively.

Some reconstructions attained adopting the present method are reported in figures 8–10 where we have represented the conductivity distribution by means of the negative contrast function componentwise defined as

$$\chi_k = \frac{\sigma_{AI} - \sigma_k}{\sigma_{AI}}. \tag{20}$$

Despite the severe ill-posedness of this inverse problem, the results show that conductivity profiles are satisfactory assessed in few Gauss–Newton iterations. The quality of the reconstruction deteriorates in the deeper layers and for high conductivity defects, as expected from the physics of the eddy currents inspection. For the sake of completeness, here we compare the results obtained by means of the proposed method with the results obtained by applying the regularization in the ‘classical’ way. In particular, we first find the minimum σ_α of

$$\mathcal{E}_{TV}(\sigma) = \|F(\sigma) - \hat{v}^*\|^2 + \alpha TV(\sigma) \tag{21}$$

for prescribed values of α . Then, we chose the regularization parameter by means, for instance, of the L-curve method [26]. Figure 11 shows the plot of the discrepancy versus the TV term corresponding to σ_α , for α in the range $[10^{-24}, 10^{-14}]$. In the L-curve method, the value of the regularization parameter is associated with the point of highest curvature. In this case,

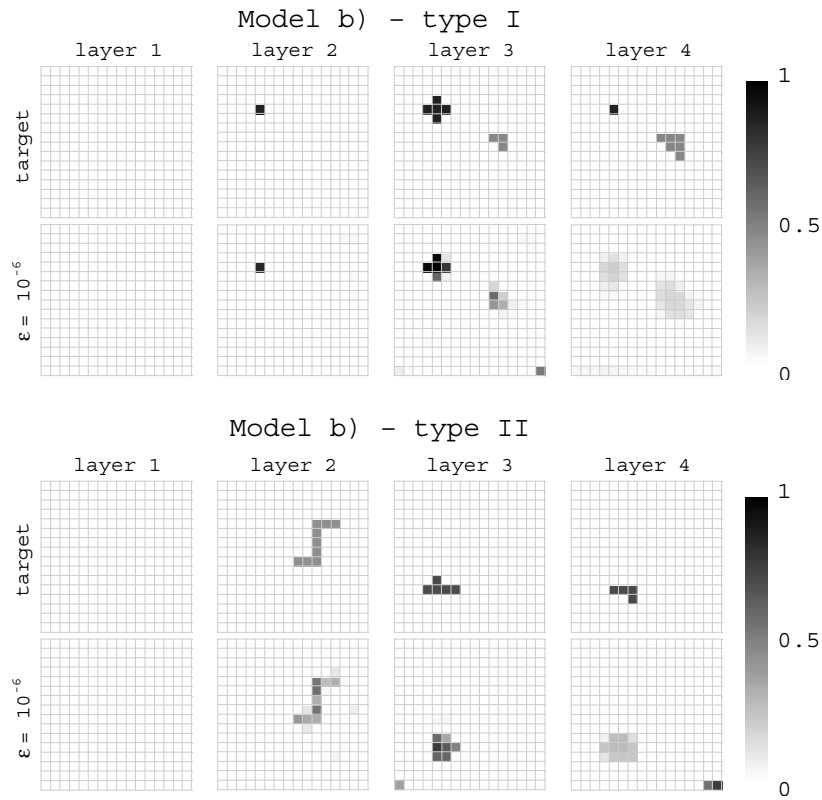


Figure 10. Images attained for model (b): the first rows report the target conductivity distributions for two types of defect; the second rows report the corresponding distributions attained for $\epsilon = 10^{-6}$ at the final iteration $n = 3, 4$ for types I and II, respectively.

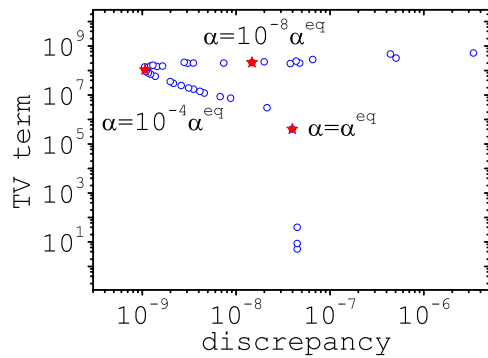


Figure 11. L-curve analogous for the TV regularization for defect model (a)—type I, with $\epsilon = 10^{-5}$.

we find $\alpha_{L\text{-curve}} = 2.52 \times 10^{-4} \times \alpha_{eq}$ that, incidentally, is in compliance with the selection rule ($10^{-3} \leq \alpha/\alpha_{eq} \leq 10^{-5}$, see section 4.1) of the proposed method. Figure 12 reports the images attained for the same defect type exploiting our and the L-curve method. It is worth noting that the proposed method leads to a less blurred reconstruction.

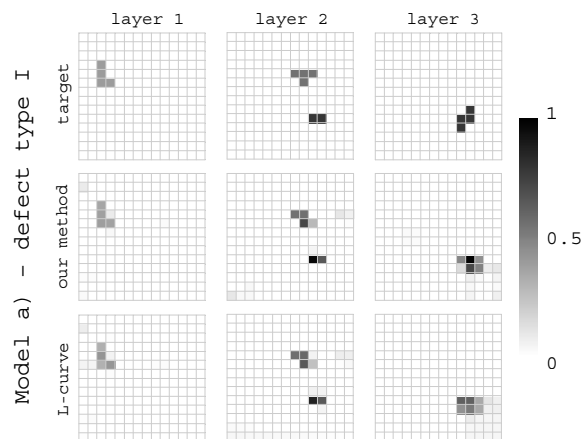


Figure 12. Images attained for model (a)—type I, with $\epsilon = 10^{-5}$: the first row reports the target conductivity distribution; rows 2,3 report the distributions attained at the final iteration $n = 3$, 3 with our method and the L-curve one, respectively.

6. Conclusions

We presented a method for solving the inverse problem of defect identification in conducting materials by eddy-current testings. The data consist of ECT measurements at several multiple frequencies to increase the information content of the data and for better forming an image of the defects at different depths. The TV regularization has been applied to each iteration of the underlying Gauss–Newton method and an appropriate rule for selecting the regularization parameter has been proposed. Moreover, a comparison with the ‘standard’ TV-based inversion method shows the superior performances of the proposed approach. Finally, a number of numerical experiments demonstrate that the proposed methodology is capable to identify the defects in few iterations with a good accuracy.

Acknowledgments

This work was partially supported by the Italian Ministry of University (MIUR-PRIN grant no 2004095237), the ‘Fondazione Cassa di Risparmio di Terni e Narni’ and the CREATE consortium, Italy.

References

- [1] Colton D and Paivarinta L 1992 The uniqueness of a solution to an inverse scattering problem for electromagnetic waves *Arch. Ration. Mech. Anal.* **119** 59–70
- [2] Isakov V 1993 Uniqueness and stability in multidimensional inverse problems *Inverse Problems* **9** 579–621
- [3] Yamamoto M 1997 A mathematical aspect of inverse problems for non-stationary Maxwell’s equations *Int. J. Appl. Electromagn. Mech.* **8** 77–98
- [4] Tamburrino A and Rubinacci G 2006 Fast methods for quantitative eddy-current tomography of conductive materials *IEEE Trans. Magn.* **42** 2017–28
- [5] Pierri R and Tamburrino A 1997 On the local minima problem in conductivity imaging via a quadratic approach *Inverse Problems* **13** 1547–68
- [6] Rubinacci G, Tamburrino A and Ventre S 1999 A differential formulation based on a perturbative approach to solve the ECT inverse problem *Comput. Methods Appl. Mech. Eng.* **169** 407–24

- [7] Dos Reis D, Lambert M and Lesselier D 2002 Non-destructive evaluation of 3-D voids in a metal plate *Inverse Problems* **18** 1857–71
- [8] Premel D and Baussard A 2002 Eddy-current evaluation of three dimensional flaws in flat conductive materials using a Bayesian approach *Inverse Problems* **18** 1873–89
- [9] Bowler J R 2002 Thin-skin eddy current inversion for the determination of crack shapes *Inverse Problems* **18** 1891–905
- [10] Luong B and Santosa F 1998 Quantitative imaging of corrosion in plates by eddy current methods *SIAM J. Appl. Math.* **58** 1509–31
- [11] Monebhurrin V, Duchêne B and Lesselier D 1998 Three-dimensional inversion of eddy current data for non-destructive evaluation of steam generator tubes *Inverse Problems* **14** 707–24
- [12] Badics Z, Pavo J, Komatsu H, Kojima S, Matsumoto Y and Aoki K 1998 Fast flaw reconstruction from 3D eddy current data *IEEE Trans. Magn.* **34** 5
- [13] Yue Li, Udpa L and Udpa S S 2004 Three-dimensional defect reconstruction from eddy-current NDE signals using a genetic local search algorithm *IEEE Trans. Magn.* **40** 2
- [14] Yin W, Dickinson S J and Peyton A J 2005 Imaging the continuous conductivity profile within layered metal structures using inductance spectroscopy *IEEE Sensors J.* **5** 2
- [15] Nair S M and Rose J H 1990 Reconstruction of three-dimensional conductivity variations from eddy current (electromagnetic induction) data *Inverse Problems* **6** 1007–30
- [16] Qi-Nian J 2000 On the iteratively regularised Gauss–Newton method for solving nonlinear ill-posed problems *Math. Comput.* **69** 1603–23
- [17] Rudin L I, Osher S and Fatemi E 1992 Nonlinear total variation noise removal algorithms *Proc. 11th Annual Int. Conf. the center for Nonlinear Studies* vol 60 pp 259–68
- [18] Vogel C R 2002 *Computational Methods for Inverse Problems* vol 23 (SIAM: Frontiers in Applied Mathematics)
- [19] Li Y and Santosa F 1996 A computational algorithm for minimizing total variation in image restoration *IEEE Trans. Image Process.* **5** 6
- [20] Acar R and Vogel C R 1994 Analysis of bounded variation penalty methods for ill-posed problems *Inverse Problems* **10** 1217–29
- [21] Strong D Chang T 2003 Edge-preserving and scale-dependent properties of total variation regularization *Inverse Problems* **19** S165–87
- [22] Soleimani M, Lionheart W R B, Peyton A J, Ma X and Higson S R 2006 A Three-dimensional inverse finite-element method applied to experimental eddy-current imaging data *IEEE Trans. Magn.* **42** 1560–7
- [23] van den Berg P M, van Broekhoven A L and Abubakar A 1999 Extended contrast source inversion *Inverse Problems* **15** 1325–44
- [24] Abubakar A and van den Berg P M 2001 Total variation as a multiplicative constraint for solving inverse problems *IEEE Trans. Image Process.* **10** 1384–92
- [25] Dobson D C and Santosa F 1994 An image enhancement technique for electrical impedance tomography *Inverse Problems* **10** 317–34
- [26] Hansen P C 1992 Analysis of discrete ill-posed problems by means of the L-curve *SIAM Rev.* **34** 561–80
- [27] Pirani A, Ricci M, Tamburrino A and Ventre S 2007 3D Reconstruction of flaws in metallic materials by eddy currents inspections *Conf. ENDE 2007* at press
- [28] Morozov M, Rubinacci G, Tamburrino A and Ventre S 2006 Numerical models of volumetric insulating cracks in eddy-current testing with experimental validation *IEEE Trans. Magn.* **42** 1568–76
- [29] Bowler J R, Jenkins S A, Sabbagh L D and Sabbagh H A 1991 Eddy-current probe impedance due to a volumetric flaw *J. Appl. Phys.* **70** 1107–14
- [30] Badics Z, Pavo J, Matsumoto Y and Komatsu H 2000 Forward solution speed-up for 3D eddy current inversion *IEEE Trans. Magn.* **36** 1124–7
- [31] Bossavit A 1998 How weak is the weak solution in finite element methods? *IEEE Trans. Magn.* **34** 2429–32
- [32] Bossavit A and Kettunen L 2000 Yee-like schemes on staggered cellular grids: a synthesis between FIT and FEM approaches *IEEE Trans. Magn.* **36** 861–7
- [33] Clemens M and Weiland T 1999 Transient eddy current calculation with the FI-method *IEEE Trans. Magn.* **35** 1163–5
- [34] Clemens M and Weiland T 2001 *Discrete Electromagnetism with the Finite Integration Technique* (PIER 32) ed F L Teixeira (Cambridge, MA: EMW Publishing) pp 65–87
- [35] Tonti E 2002 Finite formulation of the electromagnetic field *IEEE Trans. Magn.* **38** 333–6
- [36] Tonti E 1998 Algebraic topology and computational electromagnetism *4th Int. Workshop on Electric and Magnetic Fields Marseille (Fr) 12–15 May 1988* pp 284–94
- [37] Tonti E 1995 On the geometrical structure of electromagnetism Gravitation *Electromagnetism and Geometrical Structures for the 80th birthday of A. Lichnerowicz* ed G Ferrarese (Bologna Italy: Pitagora Editrice) pp 281–308

- [38] Trevisan F 2004 3-D eddy current analysis with the cell method for NDE problems *IEEE Trans. Magn.* **40** 1314–7
- [39] Cardelli E, Faba A, Specogna R and Trevisan F 2006 Reconstruction of defects in metallic plates using a multi-frequency detector system and a discrete geometric approach *IEEE Trans. Magn.* **43** 1857–60
- [40] Trevisan F and Kettunen L 2006 Geometric interpretation of finite dimensional eddy current formulations *Int. J. Numer. Methods Eng.* **67** 1888–908
- [41] Specogna R and Trevisan F 2005 Discrete constitutive equations in $A - \chi$ geometric eddy-current formulation *IEEE Trans. Magn.* **41** 1259–63
- [42] Codecasa L, Specogna R and Trevisan F 2007 Symmetric positive-definite constitutive matrices for discrete eddy-current problems *IEEE Trans. Magn.* **42** 510–5
- [43] Codecasa L and Trevisan F 2006 Piecewise uniform bases and energetic approach for discrete constitutive matrices in electromagnetic problems *Int. J. Numer. Methods Eng.* **65** 548–65
- [44] Cardelli E, Faba A, Specogna R, Tamburrino A, Trevisan F and Ventre S 2005 Analysis methodologies and experimental benchmarks for ECT *IEEE Trans. Magn.* **41** 1380–3
- [45] Tarhasaari T, Kettunen L and Bossavit A 1999 Some realizations of a discrete Hodge operator: a reinterpretation of finite element techniques *IEEE Trans. Magn.* **35** 1494–7
- [46] Durand E 1968 *Magnetostatique* (Paris: Masson & C)
- [47] Tikhonov A N and Arsenin V A 1977 *Solution of Ill-posed Problems* (Winston & Sons)
- [48] Bertero M and Boccacci P 1997 *Inverse Problems in Imaging* (Bristol: Institute of Physics Publishing)
- [49] Engl H W and Hanke M 1996 *Regularization of Inverse Problems* (Dordrecht: Kluwer)
- [50] Tarantola A 2005 *Inverse Problem Theory (Society for Industrial and Applied Mathematics)* pp 203–23
- [51] Vogel C R and Oman M E 1996 Iterative methods for total variation denoising *SIAM J. Sci. Comput.* **17** 227–38
- [52] Vogel C R and Oman M E 1998 Fast, robust total variation-based reconstruction of noisy *Blurred Images* *IEEE Trans. Magn.* **7** 6
- [53] Golub G H, Heath M and Wahba G 1978 Generalized cross-validation as a method for choosing a good ridge parameter *Technometrics* **21** 215–23
- [54] Norton S J and Bowler R J 1992 Theory of eddy current inversion *J. Appl. Phys.* **73** 501–12
- [55] Dyck D N, Lowther D A and Freeman E M 1994 A method of computing the sensitivity of electromagnetic quantities to changes in materials and sources *IEEE Trans. Magn.* **30** 5
- [56] Menke W 1989 *Geophysical Data Analysis: Discrete Inverse Theory* (New York: Academic) pp 51–5
- [57] Lebrun B, Jayet Y and Baboux J C 1997 Pulsed eddy current signal analysis: application to the experimental detection and characterization of deep flaws in highly conductive materials *NDT E Int.* **30** 163–70
- [58] Safizadeh M S, Lepine B A, Forsyth D S and Fahr A 2001 Time-frequency analysis of pulsed eddy current signals *J. Nondestruct. Eval.* **20** 73–86
- [59] Sophian A, Tian G Y, Taylor D and Rudlin J 2002 Design of a pulsed eddy current sensor for detection of defects in aircraft lap-joints *Sensors Actuators: A. Phys.* **101** 92–8
- [60] Burrascano P, Carpentieri M, Pirani A and Ricci M 2006 Galois sequences in the non-destructive evaluation of metallic materials *Meas. Sci. Technol.* **17** 2973–9